HAL
open science

Multiscale seismic reflectivity of shallow thermoclines

S. Ker, Yves Le Gonidec, L. Marié, Y. Thomas, Dominique Gibert

To cite this version:

S. Ker, Yves Le Gonidec, L. Marié, Y. Thomas, Dominique Gibert. Multiscale seismic reflectivity of shallow thermoclines. Journal of Geophysical Research. Oceans, 2015, 120 (3), pp.1872-1886 10.1002/2014JC010478 . insu-01117556

HAL Id: insu-01117556

https://insu.hal.science/insu-01117556

Submitted on 1 Apr 2016

HAL is a multi-disciplinary open access archive for the deposit and dissemination of scientific research documents, whether they are published or not. The documents may come from teaching and research institutions in France or abroad, or from public or private research centers.

L'archive ouverte pluridisciplinaire **HAL**, est destinée au dépôt et à la diffusion de documents scientifiques de niveau recherche, publiés ou non, émanant des établissements d'enseignement et de recherche français ou étrangers, des laboratoires publics ou privés.

AGU PUBLICATIONS

JGR

Journal of Geophysical Research: Oceans

RESEARCH ARTICLE

10.1002/2014JC010478

Key Points:
- A wavelet-based seismic method is extended to thermocline-related reflectors
- An analytical seismic reflectivity is developed for a simple thermocline model
- Recommendations are suggested to improve thermocline seismic detection

Correspondence to:
S. Ker,
stephan.ker@ifremer.fr

Citation:
Ker, S., Y. Le Gonidec, L. Marié, Y. Thomas, and D. Gibert (2015), Multiscale seismic reflectivity of shallow thermoclines, *J. Geophys. Res. Oceans*, *120*, 1872–1886, doi:10.1002/2014JC010478.

Received 30 SEP 2014
Accepted 9 FEB 2015
Accepted article online 14 FEB 2015
Published online 20 MAR 2015

Multiscale seismic reflectivity of shallow thermoclines

S. Ker[1], Y. Le Gonidec[2], L. Marié[3], Y. Thomas[1], and D. Gibert[2]

[1]IFREMER, Géosciences Marines, Centre de Brest, F-29280 Plouzané, France, [2]Géosciences Rennes (CNRS UMR 6118), Université Rennes 1, Rennes, France, [3]Laboratoire de Physique des Océans, UMR 6523 CNRS/IFREMER/IRD/UBO, Plouzané, France

Abstract Seismic oceanography is coming of age as an established technique of observation of the thermohaline structure of the ocean. The present paper deals with the seismic reflectivity of the Armorican Shelf seasonal thermocline, west of France, based on two seismic experiments performed with a sparker source. The peak frequency was 500 Hz for the ASPEX experiment, where the thermocline was located at 27 m water depth, and reduced to 400 Hz associated to a higher source level for the IFOSISMO experiment, where the thermocline was 12 m deeper. Despite these settings, only the first experiment could clearly highlight the thermocline reflector, providing the first seismic observation of a shallow oceanic structure. To better understand the limitation of high-resolution seismic devices in detecting weak oceanic features, we develop a wavelet-based seismic analysis and consider, as a first approximation, a simple thermocline modeled by a Gauss error function, allowing an analytical expression for the associated seismic reflectivity. We show that the acoustic impedance profile of the thermocline is mainly controlled by a sound velocity proportional to the temperature. We show that the seismic reflectivity is controlled by the reflection coefficient of the large-scale structure of the thermocline and by an attenuation factor which depends on the ratio between the seismic wavelength and the characteristic size of the thermocline. Depending on this ratio, the strength of the thermocline-related reflection may be too weak to be detected by seismic measurement.

1. Introduction

The Ocean Surface Boundary Layer (OSBL) controls the exchange of heat, momentum, and gases between the atmosphere and ocean. As such, it is a key component of the climate system, and developing a thorough understanding of its dynamics, though experimentally very challenging, is a pressing scientific issue. Even harder to observe are actually the so-called "entrainment" processes occurring at the base of the mixed layer [*Johnston and Rudnick*, 2009; *Grant and Belcher*, 2011], out of grasp of satellite observation, and which in turn control the exchanges of the OSBL with the bulk of the water column.

Ship-borne acoustic Doppler current profilers can provide measurements of current velocity at resolutions adequate for the study of these entrainment processes, but their accuracy is still marginal, and the interpretation is hampered by the lack of corresponding observations of density structure. In situ towed instruments [see, e.g., *Brown et al.*, 1996], which provide direct measurements of thermohaline properties, are currently limited to spatial resolutions on the order of one to two profiles per kilometer, which are insufficient to represent small-scale processes such as internal waves and the decameter-scale coherent structures they energize on the mixed-layer base. Microstructure measurements [see, e.g., *Soloviev et al.*, 1988; *Moum et al.*, 1995] can provide profiles of turbulent kinetic energy across the mixed-layer base, as well as indirect estimates of the turbulent diffusivities of heat, momentum, and tracers, but this information lacks horizontal context, and the influence of coherent structures, such as Langmuir circulations or Kelvin-Helmholtz billows, can be missed.

Broadband acoustic backscatter measurements are a very promising technique and have permitted spectacular advances, for instance in the study of nonlinear internal waves and their role as a source of turbulent mixing and entrainment on the seasonal thermoclines of shelf seas [*Moum et al.*, 2003]. The mechanism by which high-frequency acoustic energy is backscattered is however complicated, and untangling the contributions of turbulent microstructure and suspended particles (zooplankton, notably) from the backscattered signal remains a subject of active research [*Lavery et al.*, 2010].

During the past decade, seismic reflection techniques have been successfully applied to study the thermohaline structure of the deep ocean, including small-scale thermohaline structures like thermohaline

© 2015. American Geophysical Union. All Rights Reserved.

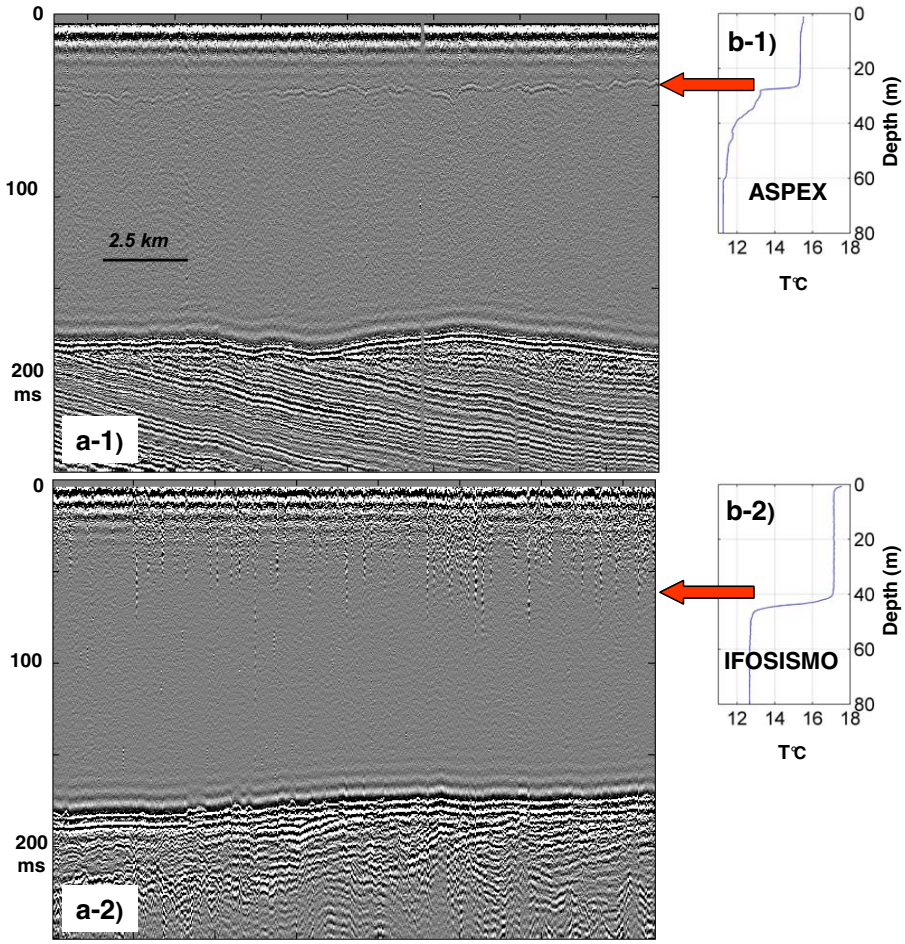

Figure 1. (a-1) Seismic profile acquired during the ASPEX cruise and (b-1) associated temperature CTD measurement [*Piété et al*., 2013]. A strong seismic reflector is clearly correlated with the main contrast of the thermocline, as pointed by the red arrow. (a-2) Seismic profile acquired during the IFOSISMO cruise and (b-2) associated temperature CTD measurement [*Thomas et al*., 2013]. In that case, even performed with the same HR seismic device, no seismic reflector associated to the significant thermocline interface is observed. It has to be noted that the salinity shows a value of 35.5 ± 0.1 (pss-78) for both cases and has no influence in the seismic response of the thermocline.

intrusions [*Holbrook et al*., 2003], thermohaline staircases [*Biescas et al*., 2010; *Fer et al*., 2010], internal gravity waves [*Holbrook and Fer*, 2005; *Holbrook et al*., 2009], and mesoscale structures like eddies [*Biescas et al*., 2008; *Ménesguen et al*., 2012] and current flows [*Mirshak et al*., 2010]. The acoustic reflectivity is essentially governed by the vertical variations of acoustic impedance, a quantity which varies with thermohaline properties according to the seawater equation of state, with temperature usually playing a dominant role [*Sallarès et al*., 2009; *Ruddick et al*., 2009]. As a first approximation, seismic sections can thus be considered to represent maps of the vertical temperature gradient. So far, however, seismic oceanography has mainly been used to study deep ocean structures, and studies of the shallowest levels of the water column (<150 m) remain rare [*Phillips and Dean*, 1991; *Carniel et al*., 2012]. This paper addresses the question of the detectability of thermohaline structures by seismic methods, and is a follow-up of the previous study by *Piété et al*. [2013].

The work of *Piété et al*. [2013] mainly focused on the specific challenges of the use of seismic methods in the shallow water column and succeeded in providing the first seismic observations of a shallow (∼30 m deep) oceanic structure, the seasonal thermocline of the Armorican Shelf, west of France (Figure 1a-1). This previous work, however, should deserve additional investigations as 3 months later another cruise performed on the same shelf, at less than 200 km distance and using the same seismic device, failed to observe the same water mass structure [*Thomas et al*., 2013] (Figure 1a-2).

Seismic reflection coefficients associated to seasonal thermoclines have not been extensively studied yet, but according to *Piété et al*. [2013], they present a high variability, ranging from −60 down to −90 dB and

© 2015. American Geophysical Union. All Rights Reserved.

are very weak compared to those found for solid Earth reflectors (typically around −40 dB). Thus, seismic detectability of such weak thermocline-related reflectors is sensitive to the noise level present in the seismic data, introduced by the electronics of the seismic apparatus itself, by mechanical noise at the sensing elements, and by the prevailing meteorological conditions. Moreover, as already observed for deeper oceanic structures [*Hobbs et al*., 2009], the seismic reflectivity of a given property interface depends sensitively on the frequency content generated by the source device [*Piété et al*., 2013]. The aim of this article is to present a systematic study of these observations and to provide a rationalization of the relationship between the physical structure of water mass interfaces and their seismic reflectivity.

In section 2, we present the two seismic surveys and associated thermocline structures. In section 3, seismic reflectivity is introduced in relation with a thermocline interface and we present a simple yet enlightening analytical model of such interface. In section 4, we present the two main multiscale wavelet-based analysis tools, the continuous wavelet transform and the wavelet response method, which we apply to the analytical thermocline profile. The insight gained is used in section 5, where the parameters controlling the seismic reflection of a given interface are quantitatively discussed, and the separate roles played by the acoustic impedance contrast, interface thickness, and seismic source peak frequency are made clear. Section 6 then provides a discussion of the contrasting results of the two seismic acquisitions at hand and provides design guidelines to improve seismic devices devoted to thermohaline structures. We finally draw some conclusions in section 7.

2. Data Sets: The Elusive Seasonal Thermocline of the Armorican Shelf

Seismic waves reflect on acoustic impedance contrasts which can be induced by sound velocity and/or density variations. In the case of ocean water masses, the cause of these variations, i.e., the origin of seismic reflections, can be temperature and/or salinity contrasts. On the western Brittany continental shelf, two seismic reflection surveys (ASPEX and IFOSISMO) were performed in 2012 to observe the structure of the seasonal thermocline.

2.1. Description of the ASPEX Case

During the ASPEX cruise aboard the French R/V Gwen Drez in June 2012, an experimental seismic device, involving a sparker source, was tested close to the island of Belle Ile. The seismic data acquisition was performed shortly after a period of intense surface-induced mixing and a satisfactory image of the mixed-layer base could be obtained, providing the first seismic image of a shallow structure (Figure 1a-1), the seasonal thermocline [*Piété et al*., 2013].

The seasonal thermocline, observed in situ with CTD measurements with a depth sampling of 20 cm, indicates a salinity S = 35.5 (pss-78) with small variations of ±0.1. The temperature profile (Figure 1b-1) is characterized by a top layer with a constant temperature $T_0 = 15.3°C$ followed by a sharp decrease of $\Delta T = 2.1°C$ in a water layer of thickness $\Delta z = 2.4$m located at 26 m water depth. Deeper, between the bottom of the thermocline and 60 m water depth, a gentle temperature decrease by 2°C occurs. On the associated seismic profile (Figure 1a-1), strong reflection at the seafloor is observed and, close to the sea surface, a weak reflector is observed in perfect agreement with the location of the thermocline: this is the seismic signature of the main thermocline discontinuity. The sparker source signal was set with a central frequency $f_p = 500$ Hz and an emission level of 205 dB re 1μ Pa at 1 m. The fold of the stacking was 100 in order to increase the signal-to-noise ratio. Note that the acquisition conditions were very good during the cruise, i.e., the sea conditions induced a low level of ambient noise.

2.2. Description of the IFOSISMO Case

During the IFOSISMO cruise aboard the French R/V Côtes de la Manche in September 2012, the same seismic device was deployed around the island of Ushant with the same objective: image the seasonal thermocline and provide a high-resolution view of the structure of the Ushant tidal front [*Le Boyer et al*., 2009]. However, in the seismic data (Figure 1a-2), the acquisition of which followed a long period of mild weather, no acoustic reflector could be observed in correspondence with the thermocline highlighted with the CTD measurements (Figure 1b-2).

The CTD data, which also indicate a salinity S = 35.5 (pss-78) with small variations of ±0.1, reveal a top layer temperature $T_0 = 17.1°C$ and a strong temperature contrast $\Delta T = 4.5°C$ in a layer thickness $\Delta z = 8.2$m located

© 2015. American Geophysical Union. All Rights Reserved.

Table 1. Parameters of the Seasonal Thermocline Measured During the ASPEX and IFOSISMO Cruises

	ΔT (°C)	T_0 (°C)	Δz (m)	z (m)	Freq (Hz)	Source Level (dB re 1μ Pa at 1 m)
ASPEX	2.1	15.3	2.4	27	500	205
IFOSISMO	4.5	17.1	8.2	39	400	208

at the water depth 39 m. As an empirical approach to improve this seasonal thermocline detection with seismic experiments, new acquisition parameters of the sparker source were set to compensate for the attenuation of the seismic wave with depth: this includes a frequency as low as $f_p = 400$ Hz and a higher emission level of 208 dB re 1μ Pa at 1 m. The fold of the stacking was set as the one of the previous case in order to insure the same sensitivity of the system as described in *Piété et al*. [2013]. But despite these settings, the seismic detection of the thermocline interface did not succeed: the thermocline reflector was too weak to be highlighted with the seismic measurements.

2.3. Rationale of the Study

These observations show that detecting a seasonal thermocline with seismic measurements is not straightforward and requires optimizing seismic acquisition settings (Table 1 sums up the different physical parameters introduced above for the IFOSISMO and ASPEX seismic cruises). On one hand, ambient and electronic noise cannot be ignored and increasing seismic source level is not a practical option because of specific technological limitations of the source devices. All these factors are detrimental to the sensitivity of the seismic device to weak reflection on thermohaline interfaces. On the other hand, it is well known that the interaction between a seismic wave and a complex seismic reflector depends on the frequency of the source signal, as introduced in the next section. To better understand seismic detectability, which represents a key point in designing seismic experiments deployed at sea to observe oceanic features, we also introduce a simple model to approximate a thermocline-related reflector used to both develop and discuss the multiscale analysis described in section 4.

3. Seismic Wave Reflected by a Thermocline Interface

3.1. Seismic Reflectivity

As a general introduction, we consider acoustic waves propagating in a fluid characterized by a vertical acoustic impedance profile $\gamma(z)=v(z)\rho(z)$, z being the depth, v the sound velocity, and ρ the density. A contrast between $\gamma(z)$ and $\gamma(z+dz)$ induces an acoustic reflectivity profile expressed by $\eta(z)=\frac{1}{2\gamma(z)}\frac{d\gamma(z)}{dz}$. Seismic reflection is thus a sonography technique that provides an image of acoustic impedance contrasts [*Yilmaz*, 1987]. In the time domain of seismic reflection, the two-way travel time for a seismic source-receiver located at the sea surface is $t(z)=2\int_0^z v^{-1}(\xi)\mathrm{d}\xi$, and the expression of the acoustic reflectivity in the single scattering approximation is $\eta(t)=\frac{1}{2}\frac{d\ln\gamma(t)}{dt}$ [*Gray and Bleistein*, 1986]. In the case of water columns in oceans, sound velocity and density, and thus γ, are both related to the temperature T, salinity S, and water depth z, through the equation of state of seawater [*Millero et al*., 1980]. If the influence of density changes can be neglected with respect to sound velocity changes in $\gamma(z)$, the reflectivity can be expressed as a spatial derivative of the sound velocity profile: $\eta(t)=\frac{1}{4}\frac{\mathrm{d}}{\mathrm{d}z}v[z(t)]$. If we further assume S contrasts are negligible in the case of thermoclines, the acoustic reflectivity only depends on the temperature gradient $dT(z)/dz$ of the thermocline.

Another parameter which controls the seismic reflectivity is the wavelength λ of the acoustic wave. Indeed, considering the simple case of two successive interfaces, the respective reflected waves can interact constructively or destructively depending on λ relative to the distance between the interfaces which is the characteristic size of the reflector. As a consequence, the reflective properties of a thermocline have to be analyzed both in time and frequency, to be able to distinguish the signatures of the different seismic impedance interfaces and the responses at the different frequencies contained in the probing signal, respectively.

© 2015. American Geophysical Union. All Rights Reserved.

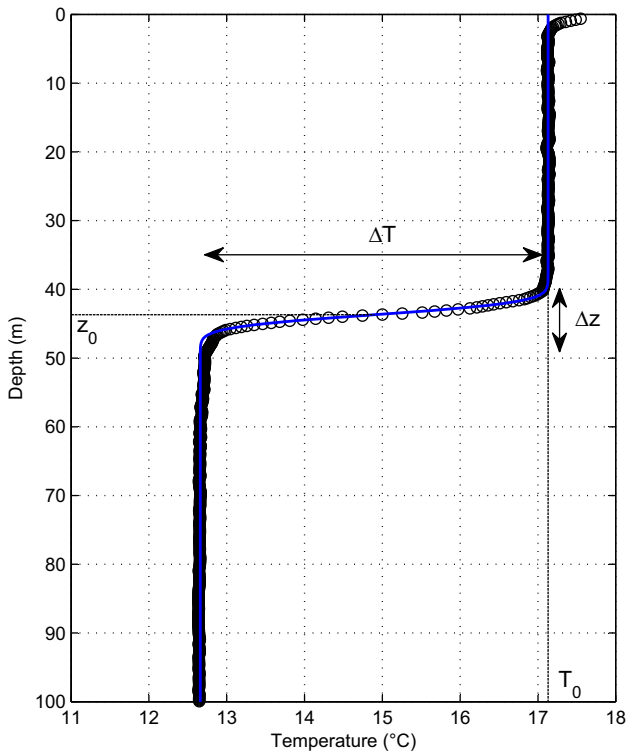

Figure 2. Seasonal thermocline measured during the IFOSISMO cruise (black circles) and the analytical GEF thermocline (blue line) based on a Gauss error function. The thermocline's parameters are shown: top layer temperature T_0, temperature contrast ΔT, thermocline thickness Δz, and depth z_0 of the thermocline's barycenter.

3.2. Analytical Thermocline Model

An analytical model to approximate a thermocline morphology, simple enough to permit an exact and illustrative analysis, can be constructed as follows. As a first approximation, a thermocline is an oceanic interface located between two water layers of different temperatures, T_0 and $T_0-\Delta T$, where the temperature contrast $\Delta T > 0$. If the discontinuity is a step-like function located at the water depth z_0, the temperature profile is expressed by:

$$T(z)=\begin{cases} T_0 & \text{if } z \le z_0 \\ T_0-\Delta T & \text{if } z > z_0 \end{cases}. \quad (1)$$

A slightly more elaborate model which still allows analytical computations and involves a measure of thermocline thickness can be formulated using a Gauss error function [*Crank*, 1980], written GEF in the remainder of the paper:

$$T(z)=T_0-\frac{\Delta T}{2}\left(1+erf\left(\frac{z-z_0}{\Delta z/4}\right)\right). \quad (2)$$

In that case, z_0 becomes the barycenter of the interface, whose characteristic size is Δz, the scale over which 90% of the total temperature variation occurs. To illustrate the morphology of such a simple analytical GEF thermocline, we use the main physical parameters of the in situ IFOSISMO thermocline summarized in Table 1. In this particular case, it is important to observe the very good agreement between the analytical GEF and the actual IFOSISMO thermoclines (Figure 2, solid line and black circles, respectively). Actually, limitations of the GEF thermocline exist at fine scales: the effects of such fine structures, which cannot easily be included in the analytical approach of the multiscale method described below, are discussed in section 6.

As recalled above, contrasts in the temperature profile $T(z)$, defined by the temperature gradient $dT(z)/dz$, induce acoustic impedance contrasts which are responsible for seismic reflections. According to the analytical GEF thermocline presented above, this gradient is expressed by

$$\frac{\mathrm{d}T(z)}{\mathrm{d}z}=\frac{-\Delta T}{\sqrt{2\pi}}\frac{1}{\kappa\Delta z}\exp\left(\frac{-(z-z_0)^2}{2(\kappa\Delta z)^2}\right), \quad (3)$$

and defines an analytical thermocline-related seismic reflector. Note that the temperature gradient tends to $-\Delta T\delta(z-z_0)$ when $\Delta z \to 0$: in this asymptotic case, no length scale is involved, i.e., the interface is homogeneous. The general expression of the temperature gradient (equation (3)) is a Gaussian function defined by the standard deviation $\kappa\Delta z$, where $\kappa=1/(4\sqrt{2})$ and Δz is the thermocline thickness, and by the expected value z_0 which corresponds to the thermocline depth location. The existence of the characteristic size $\Delta z \neq 0$ means the analytical GEF interface is complex.

4. Multiscale Wavelet-Based Method

When the temperature profile $T(z)$ is available, with CTD measurements for instance, we can analyze its morphology at different scales of observation through the use of the generic multiscale continuous wavelet

© 2015. American Geophysical Union. All Rights Reserved.

transform, which allows describing internal (small scale) and global (large scale) structures: this is the aim of section 4.1 where we show the specific results when the $T(z)$ morphology is characterized by a Gauss error function (equation (2)). When $T(z)$ is not a priori known, we extend the approach with the wavelet response method specifically devoted to the study of acoustic reflectivity of multiscale seismic reflectors: this is the aim of section 4.2 where we highlight the relation between the seismic reflectivity and the parameters of the GEF thermocline morphology.

4.1. Continuous Wavelet Transform of the Analytical Thermocline Model

To assess the multiscale features of the analytical GEF thermocline, the Continuous Wavelet Transform (CWT) method offers a depth-scale representation of the temperature profile $T(z)$ with good depth and frequency localization [*Mallat*, 1998]. The CWT can be expressed as the convolution between $T(z)$ and a family of wavelets that enables to decompose the profile at different observation scales [*Mallat*, 1998; *Alexandrescu et al.*, 1995]:

$$W[\psi, T](z,a) = \frac{1}{a}\psi\left(\frac{z}{a}\right) * T(z), \tag{4}$$

where a is the dilation, or scale parameter, of the analyzing wavelet ψ. The wavelet is an oscillating function with vanishing moments, such as the Gaussian derivative functions, i.e., $\psi = \psi_n(z) = \frac{\mathrm{d}^n}{\mathrm{d}z^n}\exp(-z^2)$, where n is the derivative order. In that case, we can write:

$$W[\psi_n, T](z,a) = \frac{1}{a}\frac{\mathrm{d}^n}{\mathrm{d}(z/a)^n}\exp\left(-\frac{z^2}{a^2}\right) * T(z), \tag{5a}$$

$$= \frac{\mathrm{d}^{n-1}}{\mathrm{d}(z/a)^{n-1}}\exp\left(-\frac{z^2}{a^2}\right) * \frac{d}{dz}T(z), \tag{5b}$$

$$= -\Delta T\left(\frac{a}{a'}\right)^n \psi_{n-1}\left(\frac{z-z_0}{a'}\right), \tag{5c}$$

with the new dilation $a' = \sqrt{a^2 + 2(\kappa\Delta z)^2}$. The passage from equation (5a) to equation (5b) is a general property of convolutions, while the passage from equation (5b) to equation (5c) is due to the stability over convolution of Gaussian functions.

In the framework of the wavelet transform, a ridge function is defined as the absolute value of $W[\psi_n, T](z,a)$ along a given line of maxima and constitutes a sparse support of the multiscale analysis [*Mallat*, 1998; *Alexandrescu et al.*, 1995]. For a step-like thermocline interface $\Delta z = 0$ (Figure 3a-1), $W[\psi, T](z,a) = -\Delta T\psi_{n-1}\left(\frac{z-z_0}{a}\right)$: the ridge function does not depend on a and the CWT components are all Gaussian derivative functions with the order $n-1$, i.e., the integral of the analyzing wavelet ψ_n. We illustrate this result by performing the CWT with $n = 3$: the CWT presents a cone-like structure with three extrema pointing onto the singularity location [*Mallat and Hwang*, 1992] (Figure 3a-2) and the ridge function plotted in a *log*−*log* diagram (Figure 3a-3) is a straight line with a slope $\alpha = 0$ in accordance with the homogeneity degree of a step-like discontinuity [*Holschneider*, 1995].

For a finite-thickness interface $\Delta z \neq 0$ (Figure 3b-1), the CWT amplitude depends on both a and ΔT, according to equation (5c), i.e., the thermocline is a complex interface whose multiscale analysis depends nontrivially on the seismic frequency. The CWT of the GEF interface performed with $n = 3$ shows a cone-like structure pointing toward the center of the discontinuity (Figure 3b-2) but the ridge function is more complex, with an absolute amplitude given by $\Delta T\left(1 + 2\left(\frac{\kappa\Delta z}{a}\right)^2\right)^{-\frac{3}{2}}$ (Figure 3b-3). At large dilations a, the curve is characterized by a straight line with $\alpha = 0$, i.e., the GEF interface is equivalent to a step-like interface at large scales of observation. At small scales of observation, the ridge function decreases as a^3, i.e., the amplitude is strongly sensitive to the wavelet dilation.

4.2. Extension to the Seismic Reflectivity With the Wavelet Response Method

4.2.1. Introduction of the Method

Le Gonidec et al. [2002] have shown experimentally that the acoustic response of a complex interface to wavelet-shaped source signals could be well predicted by the Wavelet Response (WR) method, an

© 2015. American Geophysical Union. All Rights Reserved.

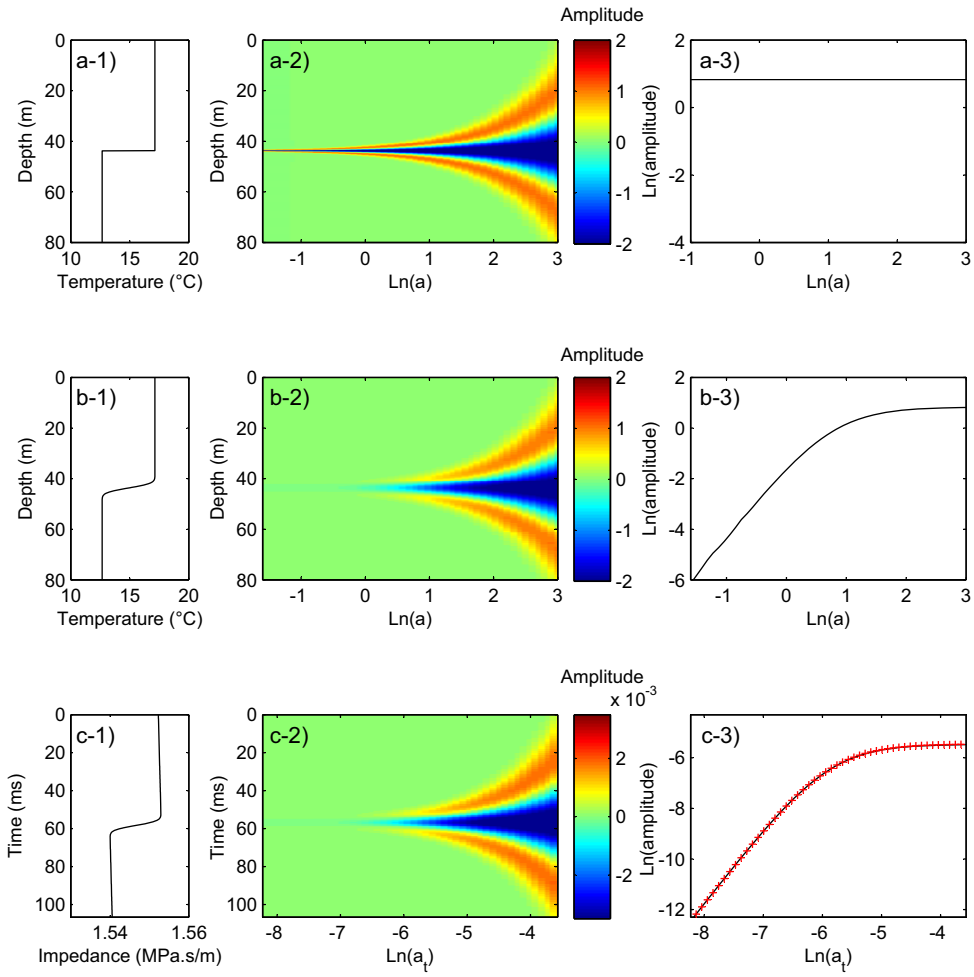

Figure 3. Step-like thermocline: (a-1) temperature profile, (a-2) CWT, and (a-3) ridge function. Analytical GEF thermocline (Gauss error function with $T_0 = 17.1°C$, $\Delta = 4.5°C$, $\Delta z = 8.2$ m, and $z_0 = 39$ m): (b-1) temperature profile, (b-2) CWT, and (b-3) ridge function. Acoustic impedance of the GEF thermocline: (c-1) profile in the TWT domain, (c-2) synthetic WR, and (c-3) ridge functions that provide the seismic reflectivity, extracted from the WR (solid line), and from the analytical solution of equation (12) (red crosses).

extension of the CWT where the convolution operator is replaced by a propagation operator $\otimes$ according to:

$$R[\psi_n, v](t, a_t) = \frac{1}{a_t}\psi_n\left(\frac{t}{a_t}\right) \otimes v(t). \tag{6}$$

The dilation a_t in the time domain controls the frequency content of the dilated wavelets: the associated wavelet peak frequency is $f_p = 1/\pi a_t$ [*Ker et al.*, 2012].

In the special case where ρ can be assumed constant and multiple scattering can be neglected, *Le Gonidec et al.* [2002] demonstrate that the WR of the sound velocity profile is equivalent to the CWT of the seismic reflectivity profile $\eta(z)$, i.e.,

$$R[\psi_n, v](t, a_t) \equiv W[\psi_n, \eta](z, a). \tag{7}$$

A perfect equivalence between both methods to analyze a sound velocity profile v is expressed by $a_t R[\psi_{n-1}, v](t, a_t) \Longleftrightarrow W[\psi_n, v](z, a)$, where $\Longleftrightarrow$ emphasizes that the WR and the CWT share the same multiscale properties although they belong to different physical spaces, i.e., time t and space z, respectively.

Currently available seismic sources cannot perform full WR measurements. Rather, each available technology can only generate a subset of the wavelets used by *Le Gonidec et al.* [2002] and *Le Gonidec and Gibert*

© 2015. American Geophysical Union. All Rights Reserved.

[2007]. In *Ker et al*. [2011], the authors extend the approach to seismic data, performing synthetic WRs based on the Goupillaud's modeling approach [*Goupillaud*, 1961] which can thus provide a full description of the acoustic response of water column interfaces at seismic wavelengths, against which available technology can be benchmarked.

4.2.2. Correspondence Between Seismic Reflectivity and Thermocline Parameters

In both our study cases, S contrasts are negligible, and the influence of density changes is negligible with respect to sound velocity changes in the acoustic impedance profile [*Piété et al*., 2013]. Linearizing the relation between v and T within the thermocline, we can establish a direct equivalence between the WR of v and the CWT of T:

$$a_t R[\psi_{n-1}, v](t, a_t) \Longleftrightarrow W[\psi_n, T](z, a). \tag{8}$$

This original result shows that the multiscale structure of a thermocline temperature profile T could be directly assessed by performing a seismic survey with source signals designed as dilated wavelets ψ_{n-1} and taking benefits of the CWT properties. According to equation (5c) and relation (8), we show that the analytical expression of the seismic WR of a GEF thermocline (equation (2)) is expressed by:

$$R[\psi_{n-1}, v](t, a_t) = r_0 \left(\frac{a_t}{a_t'}\right)^n \frac{1}{a_t'} \psi_{n-1}\left(\frac{t-t_0}{a_t'}\right). \tag{9}$$

The seismic signal reflected by the GEF thermocline insonified by a seismic wavelet ψ_{n-1} with a peak frequency $f_p = 1/\pi a_t$ is thus a similar wavelet ψ_{n-1} with modified peak frequency $1/\pi a_t'$ and dilation $a_t' = \sqrt{a_t^2 + 2\left(\frac{\kappa \Delta z}{v_{rms}}\right)^2}$, which depends on the thermocline thickness Δz and $v_{rms} = \sqrt{\frac{\sum_i v_i^2 \Delta t_i}{\sum_i \Delta t_i}}$, the root mean square sound velocity.

For a step-like thermocline $\Delta z = 0$, the ridge function of the WR (equation (9)) does not depend on the source dilation a_t as expected for this homogeneous interface [*Le Gonidec et al*., 2002]. Thus, r_0 corresponds to the reflection coefficient of the step-like thermocline-related reflector located at the two-way travel time $t_0 = 2z_0/v_{rms}$:

$$r_0 = \frac{v(T_0 - \Delta T) - v(T_0)}{v(T_0 - \Delta T) + v(T_0)}. \tag{10}$$

For a finite-thickness interface $\Delta z \neq 0$, the ridge function depends on a_t, as expected for a complex reflector, and we note

$$r = r_0 \left(\frac{a_t}{a_t'}\right)^n, \tag{11}$$

the multiscale seismic reflection coefficient of the reflector, called seismic reflectivity for the sake of simplicity in the remainder of the paper.

4.2.3. Comparison Between the Analytical Seismic Reflectivity and the Synthetic Wavelet Response

In exploration seismology, it is common to approximate the seismic source signal ψ_{n-1} of equation (9) as a Ricker signal, defined by $\frac{d^2}{dt^2}\exp(-t^2)$. For this particular application where $n = 3$, the analytical expression of the thermocline seismic reflectivity established from equation (11) is given by:

$$r = r_0 \left(1 + 2\left(\frac{\pi \kappa \Delta z}{\lambda}\right)^2\right)^{-\frac{3}{2}}, \tag{12}$$

where $\lambda = v_{rms}/f_p$ is the wavelength of the seismic source wavelet of peak frequency $f_p = 1/\pi a_t$.

We remember that the analytical expression of r given by equation (12) is based on four main approximations: a constant seawater salinity S, a constant fluid density ρ, a sound velocity $v \propto T$, and the Born approximation. The first approximation is validated by in situ CTD measurements as mentioned in section 2. To discuss the last three approximations, we now compare the analytical expression of r, based on a GEF thermocline, with the seismic reflectivity computed with a direct synthetic WR [*Ker et al*., 2011], which consists in propagating seismic wavelets ψ_2 through the acoustic impedance profile γ. This synthetic WR method allows

© 2015. American Geophysical Union. All Rights Reserved.

taking into account the full polynomial expansion of the seawater sound velocity [*Millero et al.*, 1980] (with T and z but also S for general purposes) as well as the seawater density, to define the impedance profile as a function of the exact two-way travel time (Figure 3c-1). As a first observation, the global shape of γ is similar to the temperature profile (Figure 3b-1), i.e., the acoustic impedance is actually dominated by the temperature contrasts within the thermocline structure: the slight increase of γ in the top and underlying layers is due to both surrounding pressure variations with depth and residual temperatures induced by the Gauss error function model (equation (2)). A second observation deals with the synthetic WR (Figure 3c-2) which shows a cone-like structure pointing toward the center of the discontinuity in perfect agreement with the CWT analysis (Figure 3b-2): the WR of the acoustic impedance profile performed with an analyzing wavelet ψ_2 is equivalent to the CWT of the temperature profile performed with ψ_3 as expected by the equivalence expressed by equation (8). The main ridge function extracted from the WR is plotted in a *log*−*log* diagram where we also plot the analytical seismic reflectivity (equation (12)) of the associated GEF thermocline (Figure 3c-3, solid line and red crosses, respectively). It is obvious that both curves perfectly match, without discrepancy, showing identical asymptotic behavior at large dilations and linear decrease at small dilations.

Three main conclusions can be drawn from these quantitative results about the multiscale characterization of a thermocline morphology from seismic measurements. First, the assumptions required to consider the analytical expression of the seismic reflectivity are satisfied in the context of thermocline interfaces: the multiple scattering of seismic waves by the thermocline features and the nonlinearity of the seawater sound velocity with T and z can actually be neglected. Second, the analytical expression of the seismic reflectivity of a thermocline based on a Gauss error function shape can be used to analyze the relationship between the thermocline physical parameters and the seismic reflectivity, as discussed now in section 5. Third, we highlight that the wavelet response is an efficient multiscale method to analyze general in situ thermoclines with complex morphologies, as discussed in section 6.

5. Physical Parameters Controlling the Seismic Thermocline Detectability

The seismic reflectivity given by equation (12) can be expressed in decibel (dB) as $r^{dB}=r_0^{dB}+\Lambda^{dB}$ with:

$$r_0^{dB}=20\ \log_{10}(r_0), \tag{13}$$

$$\Lambda^{dB}=-30\ \log_{10}\left(1+\left(\frac{4}{\pi}\frac{\lambda}{\Delta z}\right)^{-2}\right). \tag{14}$$

The term r_0^{dB} corresponds to the seismic reflection coefficient of a step-like interface (equation (10)) and depends on ΔT and T_0 only, not on the seismic wavelength λ. The negative term Λ^{dB} is an attenuation factor controlled by the ratio between λ and the thermocline thickness Δz, not on the thermocline temperatures.

5.1. Large-Scale Seismic Reflectivity: $r_0^{dB}(T_0, \Delta T)$

As discussed in the previous sections, the thermocline interface is equivalent to a step-like reflector at large scales of observation, i.e., when the seismic wavelength is much larger than the thermocline thickness. In that case, the asymptotic seismic reflectivity is r_0^{dB} (equation (13)) and we now discuss its sensitivity to the top layer temperature T_0 and to the temperature contrast ΔT. To do so, we consider typical temperatures of midlatitude seasonal thermoclines, i.e., the large-scale seismic reflectivity is determined for T_0 ranging between 14°C and 20°C, and for ΔT between 1°C and 6°C (Figure 4). We observe that r_0^{dB} slightly decreases with T_0 for a given ΔT and strongly increases with ΔT for a given T_0, i.e., variations of the reflection coefficient is dominated by variations of ΔT. For example with $\Delta T=1$°C, a decrease of 1 dB only is observed between $T_0=14$ and 20°C, and an increase as high as 24 dB is observed between $\Delta T=1$ and 6°C for $T_0=14$°C. Note that similar values of r_0^{dB} can be associated to different values of $(T_0, \Delta T)$, i.e., a single measurement of the large-scale seismic reflectivity is not sufficient to isolate ΔT and T_0.

5.2. Multiscale Attenuation: $\Lambda^{dB}(\lambda, \Delta z)$

At smaller scales of observations, the seismic reflectivity decreases with the seismic frequency according to the attenuation factor Λ^{dB} (equation (14)) related to the complex morphology of the thermocline-related reflector. Actually, the relevant parameter is the ratio $\lambda/\Delta z$, as already discussed in previous works with solid

© 2015. American Geophysical Union. All Rights Reserved.

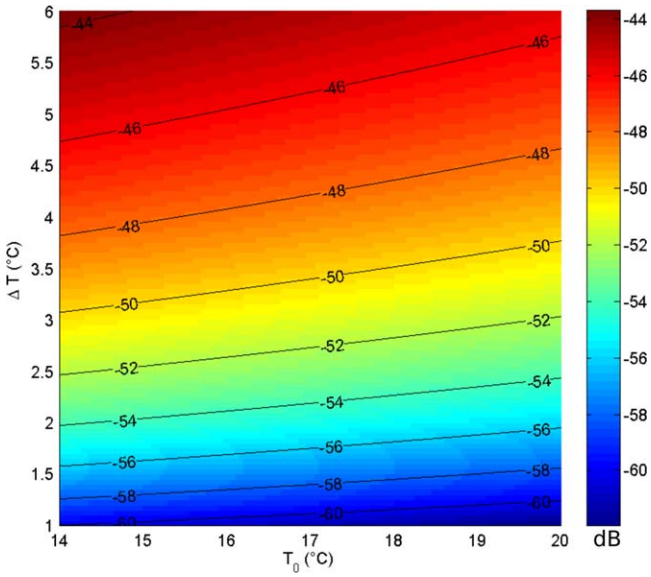

Figure 4. Large-scale reflection coefficient r_0^{dB} of an analytical GEF thermocline with a top layer temperature T_0 ranging between 14°C and 20°C and a temperature contrast ΔT between 1°C and 6°C.

Earth reflectors [*Le Gonidec et al.*, 2002; *Ker et al.*, 2012, 2014]. Thus, we determine the attenuation Λ^{dB} for typical $\lambda/\Delta z$ ranging between 0.1 up to 50 (Figure 5). As expected, the shape of the curve is equivalent to the one of the ridge function plotted as a function of a_t (Figure 3c-3), with two asymptotic behaviors: $\Lambda^{dB} \simeq 0$ dB at low frequencies where the seismic reflectivity is thus the constant large-scale reflection coefficient r_0^{dB}, and $\Lambda^{dB} \propto -60\log_{10}(\lambda/\Delta z)$ at high frequencies.

As a consequence, we can define three characteristic domains of the seismic reflectivity which depend on the nondimensional parameter $\lambda/\Delta z$. Domain I stands for the large scales of observation and is defined for $\lambda/\Delta z > 10$ where $r^{dB} = r_0^{dB}$ does not depend on the thermocline thickness. Note that this is in favor of the thermocline detectability but no information can be recovered about the multiscale structure of the thermocline. Domain III stands for the small scales of observation and is defined for $\lambda/\Delta z < 0.5$, where the seismic reflectivity strongly decreases as the cube of the seismic frequency: such very weak reflections require sensitive seismic devices and are directly related to thermocline thicknesses. Domain II, the transition zone between these two domains is defined as the mesoscales of observation where the seismic reflectivity does not depend linearly on the frequency in a *log*−*log* diagram.

5.3. Application to the Thermocline Detectability Problem

To specifically investigate the thermocline detectability problem, we perform the multiscale seismic analysis of GEF thermoclines of varying thicknesses, for which we have derived the analytical expression of the seismic reflectivity (equation (12)). The parameters of the analytical GEF thermocline are chosen to fit the IFO-SISMO thermocline (whose thickness is $\Delta z = 8.2$ m) (Figure 2), i.e., the optimized parameters are the following: a barycenter located at the water depth $z_0 = 43.7$ m, a top layer temperature $T_0 = 17.13$°C, and a temperature contrast $\Delta T = 4.47$°C. In order to study the impact of λ and Δz on the seismic reflectivity, we perform the analysis for several thicknesses ranging between 0 and 20 m and for typical seismic source peak frequencies f_p between 50 and 1000 Hz (Figure 6). Note that larger thicknesses are usually not observed for midlatitude seasonal thermoclines, lower f_p relative to z_0 have to be avoided because of interferences between the strong direct signal and the weak reflection on the thermocline (see Figure 1a), and higher frequencies usually do not insure good signal-to-noise ratio. We observe a general decreasing trend of r^{dB} with both Δz and f_p. For a given Δz, a strong variation of r^{dB} with f_p is related to a large thermocline, whereas narrow thermoclines are weakly frequency-dependent and highly reflective. Similarly, the seismic reflectivity of a wide range of thermocline thicknesses is high and nearly stable for a fixed low seismic frequency, whereas a high frequency shows a strong attenuation of the seismic reflectivity with large Δz. This highlights the seismic detectability of a thermocline: for instance, considering a sensitivity of the seismic device typically limited to −70 dB, a seismic device with $f_p = 400$ Hz is theoretically not able to detect thermoclines larger than 5 m.

6. Seismic Detection of Shallow Thermoclines in the Western Brittany Continental Shelf

The seismic multiscale analysis based on the WR approach provides a quantitative description of the seismic reflectivity associated to an analytical GEF thermocline (equation (2)). Now we extend the analysis to the

© 2015. American Geophysical Union. All Rights Reserved.

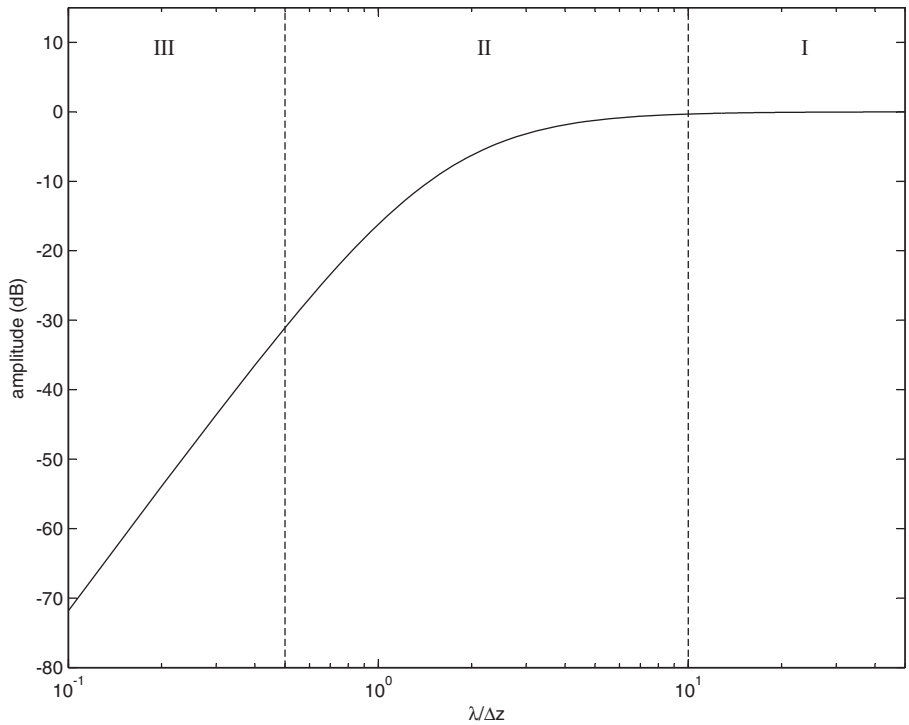

Figure 5. Multiscale attenuation Λ^{dB} as a function of the ratio between the seismic wavelength λ and the thermocline thickness Δz. Identification of three scales of observation: (I) large scales $\lambda/\Delta z > 10$, (II) mesoscales, and (III) fine scales $\lambda/\Delta z < 0.5$.

actual in situ ASPEX and IFOSISMO thermoclines, respectively, in order to better explain and discuss the seismic observations introduced in section 2.

6.1. Multiscale Analysis of the ASPEX Thermocline Observed in the Seismic Data

We consider the main physical parameters of the in situ ASPEX thermocline summarized in Table 1 to define the associated analytical GEF thermocline (Figure 7a, black and blue lines, respectively): both thermoclines are similar down to the water depth 27 m and then disagree, with a difference increasing with depth. However, the synthetic WR of the actual ASPEX thermocline displayed in Figure 7b shows a main cone-like structure pointing toward the main discontinuity, i.e., the thermocline location. Located after this dominant structure, additional weak features can be observed in the WR (see, for instance, the low-frequency content located around 60 ms) but, nevertheless, the actual thermocline looks locally equivalent to an analytical thermocline based on the Gauss error function. Accordingly, the ridge function (white dashed line) is in good agreement with the analytical seismic reflectivity r^{dB} of the associated GEF thermocline when plotted as a function of the seismic frequency (Figure 7c, black and blue lines, respectively). This

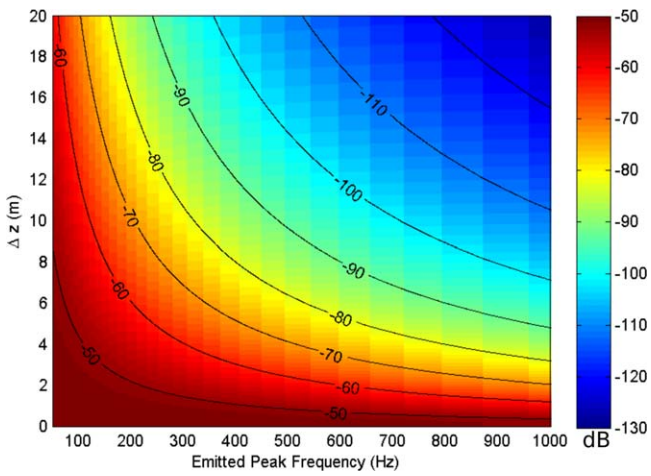

Figure 6. Seismic reflectivity r^{dB} of an analytical GEF thermocline (Gauss error function with $T_0 = 17.1°C$, $\Delta = 4.5°C$) as a function of the thermocline thickness Δz ranging between 0 and 20 m and the seismic peak frequency f_p ranging between 50 and 1000 Hz.

© 2015. American Geophysical Union. All Rights Reserved.

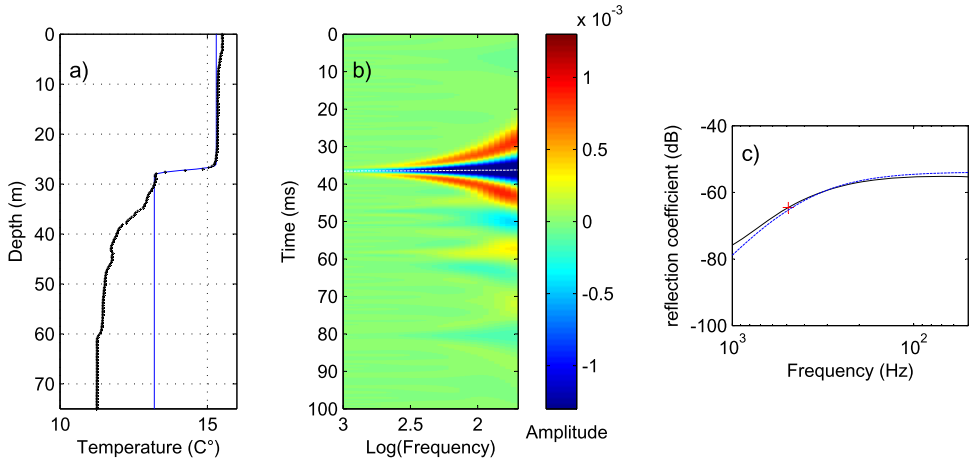

Figure 7. (a) Temperature profile of the actual thermocline measured from a CTD probe during the ASPEX cruise (black line) and associated analytical GEF thermocline (blue line). (b) Synthetic WR of the actual thermocline. (c) Seismic reflectivity of the actual thermocline extracted from the WR ridge function (black line) and analytical seismic reflectivity from the GEF thermocline (blue line). The red cross indicates the reflection coefficient at the central frequency of the ASPEX seismic device.

agreement highlights that even if the actual and GEF thermoclines do not agree at all scales of observation, the seismic reflectivity is dominated by the sharp temperature contrast of the thermocline. At low frequencies, both curves tend to an asymptotic value around −55.2 dB which corresponds to the reflection coefficient of an equivalent step-like interface. At higher frequencies, both curves similarly decrease down to −78 dB at 1000 Hz. In particular at the sparker source frequency $f_p = 500$ Hz, the reflection coefficient of the thermocline is about −64.5 dB, as predicted by the GEF thermocline. Since the ASPEX thermocline was clearly observed in the seismic data, this actual reflection coefficient is obviously above the detection limit of the seismic device, i.e., the detectability conditions were satisfied for this first seismic observation of a shallow oceanic structure. Note that in the present case characterized by a low background noise associated with good sea conditions, the detectability limit of the seismic device is thus lower than −64.5 dB.

6.2. Multiscale Analysis of the IFOSISMO Thermocline Not Observed in the Seismic Data

The plots of both the actual IFOSISMO and associated analytical GEF thermoclines are recalled in Figure 8a (black and blue lines, respectively). As already discussed in section 3.2, both curves match closely, with weak disagreements at small scales of observations. The synthetic WR of the actual thermocline is displayed in Figure 8b: a main cone-like structure points toward the center of the thermocline in accordance with the synthetic WR of the analytical GEF thermocline described in section 4.2 (Figure 3c-2). Actually, additional weak features can be observed: they are related to the fine-scale structures of the actual IFOSISMO temperature profile which are not considered in the associated GEF thermocline. The synthetic ridge function (white dashed line) is plotted as a function of the seismic frequency in Figure 8c (black line) superimposed with the analytical seismic reflectivity r^{dB} of the associated GEF thermocline (blue line). At low frequencies (<150 Hz), both curves are in good agreement, with a similar asymptotic trend, suggesting the thermocline is equivalent to a step-like interface characterized by a seismic reflection coefficient r_0^{dB} of −48.7 dB, at least. At higher frequencies, the two curves do not agree: the analytical GEF seismic reflectivity underestimates the ridge function of the IFOSISMO thermocline. This disagreement highlights that even if the actual IFOSISMO thermocline and the analytical GEF thermocline look very similar (Figure 8a), the fine-scale structures of the actual thermocline have a strong impact on the ridge function morphology, i.e., on the seismic reflectivity. In particular at the sparker source frequency $f_p = 400$ Hz, the amplitude −71.3 dB of the ridge function is 10 dB higher than the reflection coefficient predicted with a GEF thermocline. This low reflectivity of the IFOSISMO thermocline at $f_p = 400$ Hz explains the weakness of the signal reflected on the thermocline interface, a conclusion supported by the present work. But since sea conditions were not as good as in the ASPEX case, ambient noise cannot be neglected and can also contribute to the thermocline undetectability.

© 2015. American Geophysical Union. All Rights Reserved.

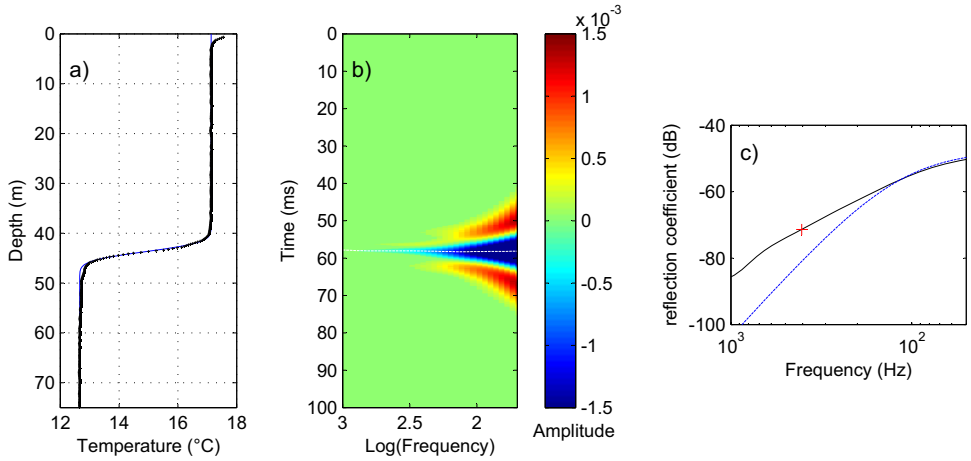

Figure 8. (a) Temperature profile of the actual thermocline measured from a CTD probe during the IFOSISMO cruise (black line) and associated analytical GEF thermocline (blue line). (b) Synthetic WR of the actual thermocline. (c) Seismic reflectivity of the actual thermocline extracted from the WR ridge function (black line) and analytical seismic reflectivity defined from the GEF thermocline (blue line). The red cross indicates the reflection coefficient at the central frequency of the IFOSISMO seismic device.

6.3. Recommendations About the Seismic Frequency

The present analysis helps to better understand why a seismic survey is able to detect a thermocline or not, as was the case for the ASPEX and IFOSISMO cruises, respectively. For the ASPEX seismic data, the acquisition conditions were optimal (see section 2.1) to detect the thermocline-related reflector, comprising a source emission level and frequency adapted to the thermocline reflective properties. For the IFOSISMO seismic data, in addition to bad sea conditions (see section 2.2) which deteriorate the signal-to-noise ratio, the thermocline reflection coefficient is two times weaker than the one of ASPEX. As a consequence, even with a higher source level which compensates for the spherical divergence of the seismic signal, the detection limit of the seismic device was not satisfied. According to the present work, the seismic source frequency appears not adapted to the thermocline morphology and explains why the thermocline-related reflector does not emerge from the noise level of the IFOSISMO seismic profile. Which recommendations about the seismic device could have been done to optimize the thermocline detection?

Taking benefits of the multiscale seismic analysis, the seismic reflectivity $r^{dB} = r_0^{dB} + \Lambda^{dB}$ of a seasonal thermocline can be determined for a wide range of seismic frequencies. At low frequencies, both the ASPEX and the IFOSISMO thermoclines are characterized by nearly similar asymptotic behaviors of the ridge functions: at large scales, r^{dB} tends to the reflection coefficient r_0^{dB} of an equivalent step-like thermocline. Note that r_0^{dB}, which mainly depends on ΔT (see section 5.1), is at least 6 dB higher for the IFOSISMO thermocline than for the ASPEX thermocline (Table 2). This suggests that low seismic frequencies are recommended to detect thermoclines, keeping in mind three main limitations: low frequencies cannot be used for superficial thermoclines because of wave interferences with the direct source signal, the lateral resolution of seismic imaging decreases at low frequencies, and last but not least, low frequencies do not inform about the thermocline morphology.

At high frequencies, r^{dB} is controlled by the ratio $\lambda/\Delta z$ following the attenuation Λ^{dB} described in section 5.2. Removing r_0^{dB} from the seismic reflectivity r^{dB}, the ridge functions of both actual thermoclines are plotted as a function of $\lambda/\Delta z$ in Figure 9 (blue diamonds and red circles, respectively). Note that considering the frequency of the seismic source signal and the thermocline thickness given in Table 1, $\lambda/\Delta z = 0.45$ for IFOSISMO and 1.25 for ASPEX, associated to an attenuation 12 dB higher for the former (Table 2). The thermocline attenuation curve (Figure 9, blue diamonds) shows a good agreement with the simple analytical model for $1 < \lambda/\Delta z < 7$: at higher frequencies, a disagreement is explained by the fine-scale features of the thermocline. This highlights the strong sensitivity of the seismic reflectivity with the seismic wavelength relative to the thermocline thickness, explaining the weak seismic signals reflected by the IFOSISMO thermocline. High frequencies inform about the thermocline morphology, but the associated attenuation might make the thermocline undetectable by the seismic measurements. If we consider the ASPEX seismic

© 2015. American Geophysical Union. All Rights Reserved.

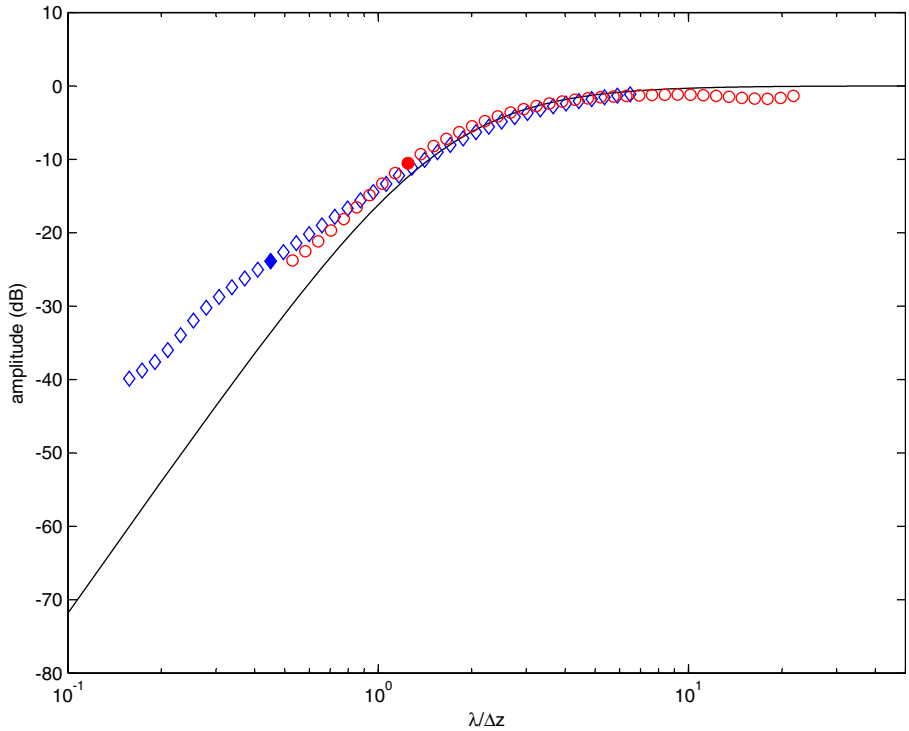

Figure 9. Seismic reflectivity as a function of the ratio between the seismic wavelength λ and the thermocline thickness Δz for the actual thermoclines of IFOSISMO (blue diamonds) and ASPEX (red circles) cruises. Note that the large-scale seismic reflectivity value has been removed. Filled symbols correspond to the ratio associated to the seismic source central frequency for both cruises. The solid line shows the multiscale attenuation Λ^{dB} of the analytical result of the GEF thermocline (equivalent to Figure 3).

reflectivity as a reference for a thermocline detectability, a seismic frequency around 180 Hz would have been in favor of the seismic observation of the IFOSISMO thermocline, i.e., the selected frequency $f_p = 400$ Hz was far too high. Note that when talking about thermocline detectability, the ambient noise level is superimposed to the weakness of the reflector described in the present paper and contributes to a poor signal-to-noise ratio.

7. Concluding Remarks

The multiscale seismic analysis based on the WR approach is an effective tool to assess the frequency-dependent reflection coefficient of shallow seasonal thermoclines. Considering a simple model of a thermocline based on both a Gauss error function and a linear relation between the sound velocity and temperature in the water column, we derive an analytical expression of the seismic reflectivity which consists in two terms: an asymptotic value at low frequencies, where the seismic reflectivity is maximum, constant, and controlled by the temperature parameters, and a frequency-dependent attenuation factor controlled by the ratio between the seismic source wavelength and the size of the thermocline.

This work allows us quantifying the influence of the thermocline morphology on the seismic reflection coefficient, i.e., a better understanding of the interaction between a seismic wave and a thermocline-like reflector. But an additional effect controls the detectability of weak reflectors: indeed, ambient noise including sea conditions limits the signal-to-noise ratio and thus the thermocline detection. To overcome this limitation, a first attempt is to increase the fold of the stacking or/and the seismic source level according to the ambient noise level mainly controlled by the wind speed [*Wenz*, 1962]. Finally, we are able to make some recommendations about seismic devices designed for seasonal thermocline detection, including

Table 2. Parameters of the Seismic Reflectivity Associated to the ASPEX and IFOSISMO Thermoclines

	r^{dB} (dB)	r_0^{dB} (dB)	Λ^{dB} (dB)	$\lambda/\Delta z$
ASPEX	−64.5	−55.2	−9.3	1.25
IFOSISMO	−71.3	−48.7	−22.6	0.45

© 2015. American Geophysical Union. All Rights Reserved.

seismic source frequency, and the present work should contribute to a better knowledge of the spatial distribution and circulation of water masses in the ocean.

Acknowledgments
It is a pleasure to thank the captains and crews of R/V Gwen Drez and R/V Côte de la Manche, who made the data collection possible. The authors thank B. Marsset for the acquisition of IFOSISMO and ASPEX seismic data sets. We also thank C. Ménesguen for constructive discussions. Please note that CTD and seismic data used in this article still belong exclusively to IFREMER and are not available at the present time.

References

Alexandrescu, M., D. Gibert, G. Hulot, J.-L. L. Mouël, and G. Saracco (1995), Detection of geomagnetic jerks using wavelet analysis, *J. Geophys. Res.*, *100*, 12,557–12,572.
Biescas, B., V. Sallarès, J.-L. Pelegrí, F. Machín, R. Carbonell, G. Buffett, J.-J. D. Nobeitia, and A. Calahorrano (2008), Imaging meddy finestructure using multichannel seismic reflection data, *Geophys. Res. Lett.*, *35*, L11609, doi:10.1029/2008GL033971.
Biescas, B., L. Armi, V. Sallarès, and E. Gràcia (2010), Seismic imaging of staircase layers below the Mediterranean Undercurrent, *Deep Sea Res., Part I*, *57*, 1345–1353.
Brown, J., K. Brander, L. Fernand, and A. E. Hill (1996), Scanfish: High performance towed undulator, *Sea Technol.*, *37*, 23–27.
Carniel, S., A. Bergamasco, J. W. Book, R. W. Hobbs, M. Sclavo, and W. T. Wood (2012), Tracking bottom waters in the Southern Adriatic Sea applying seismic oceanography techniques, *Cont. Shelf Res.*, *44*, 30–38.
Crank, J. (1980), *The Mathematics of Diffusion*, Oxford Univ. Press. Oxford, U. K.
Fer, I., P. Nandi, W. Holbrook, R. Schmitt, and P. Pàramo (2010), Seismic imaging of a thermohaline staircase in the western tropical North Atlantic, *Ocean Sci.*, *6*, 621–631.
Goupillaud, P. (1961), An approach to inverse filtering of near-surface layer effects from seismic records, *Geophysics*, *26*, 754–760.
Grant, A. L. M., and S. E. Belcher (2011), Wind-driven mixing below the oceanic mixed layer, *J. Phys. Oceanogr.*, *41*, 1556–1575.
Gray, S. H., and N. Bleistein (1986), Imaging and inversion of zero-offset seismic data, *Proc. IEEE*, *74*, 440–456.
Hobbs, R. W., D. Klaeschen, V. Sallarès, E. Vsemirnova, and C. Papenberg (2009), Effect of seismic source bandwidth on reflection sections to image water structure, *Geophys. Res. Lett.*, *36*, L00D08, doi:10.1029/2009GL040215.
Holbrook, W. S., and I. Fer (2005), Ocean internal wave spectra inferred from seismic reflection transects, *Geophys. Res. Lett.*, *32*, L15604, doi:10.1029/2005GL023733.
Holbrook, W. S., P. Pàramo, S. Pearse, and R. Schmitt (2003), Thermohaline fine structure in an oceanographic front from seismic reflection profiling, *Science*, *301*, 821–824.
Holbrook, W. S., I. Fer, and R. Schmitt (2009), Images of internal tides near the Norwegian continental slope, *Geophys. Res. Lett.*, *36*, L00D10, doi:10.1029/2009GL038909.
Holschneider, M. (1995), *Wavelets: An Analysis Tool*, Clarendon, Oxford, U. K.
Johnston, T. M. S., and D. L. Rudnick (2009), Observations of the transition layer, *J. Phys. Oceanogr*, *39*, 780–797.
Ker, S., Y. Le Gonidec, D. Gibert, and B. Marsset (2011), Multiscale seismic attributes: A wavelet-based method and its application to high-resolution seismic and ground truth data, *Geophys. J. Int.*, *187*, 1038–1054.
Ker, S., Y. Le Gonidec, and D. Gibert (2012), Multiscale seismic attributes: Source-corrected wavelet response and its application to high-resolution seismic data, *Geophys. J. Int.*, *190*, 1746–1760.
Ker, S., Y. Le Gonidec, B. Marsset, G. Westbrook, D. Gibert, and T. A. Minshull (2014), Fine-scale gas distribution in marine sediments assessed from deep-towed seismic data, *Geophys. J. Int.*, *196*, 1466–1470.
Lavery, A., D. Chu, and J. N. Moum (2010), Observations of broadband acoustic backscattering from nonlinear internal waves: Assessing the contribution from microstructure, *IEEE J. Oceanic Eng.*, *35*(4), 695–709.
Le Boyer, A., G. Cambon, N. Daniault, S. Herbette, B. L. Cann, L. Marié, and P. Morin (2009), Observations of the Ushant tidal front in September 2007, *Cont. Shelf Res.*, *29*, 1026–1037.
Le Gonidec, Y., and D. Gibert (2007), Multiscale analysis of waves reflected by granular media: Acoustic experiments on glass beads and effective medium theories, *J. Geophys. Res.*, *112*, B05103, doi:10.1029/2006JB004518.
Le Gonidec, Y., D. Gibert, and J.-N. Proust (2002), Multiscale analysis of waves reflected by complex interfaces: Basic principles and experiments, *J. Geophys. Res.*, *107*(B9), 2184, doi:10.1029/2001JB000558.
Mallat, S. (1998), *A Wavelet Tour of Signal Processing*, 2nd ed., Academic, Burlington, Vermont.
Mallat, S., and W. L. Hwang (1992), Singularity detection and processing with wavelets, *IEEE Trans. Inf. Theory*, *38*, 617–643.
Ménesguen, C., B. Hua, X. Carton, F. Klingelhoefer, P. Schnurle, and C. Reichert (2012), Arms winding around a meddy seen in seismic reflection data close to the Morocco coastline, *Geophys. Res. Lett.*, *39*, L05604, doi:10.1029/2011GL050798.
Millero, F. J., C. Chen, A. Bradshaw, and K. Schleicher (1980), A new high pressure equation of state for seawater, *Deep Sea Res., Part A*, *27*, 255–264.
Mirshak, R., M. R. Nedimovic, B. J. W. Greenan, B. Ruddick, and K. Louden (2010), Coincident reflection images of the gulf stream from seismic and hydrographic data, *Geophys. Res. Lett.*, *37*, L05602, doi:10.1029/2009GL042359.
Moum, J. N., M. C. Gregg, R. C. Lien, and M. E. Carr (1995), Comparison of turbulence kinetic energy dissipation rate estimates from two ocean microstructure profilers, *J. Atmos. Oceanic Technol.*, *12*, 346–366.
Moum, J. N., D. M. Farmer, W. D. Smyth, L. Armi, and S. Vagle (2003), Structure and generation of turbulence at interfaces strained by internal solitary waves propagating shoreward over the continental shelf, *J. Phys. Oceanogr.*, *33*, 2093–2112.
Phillips, J. D., and D. Dean (1991), Multichannel acoustic reflection profiling of ocean watermass temperature/salinity interfaces, in *Ocean Variability and Acoustic Propagation*, edited by J. Potter and A. Warn-Varnas, pp. 199–214, Kluwer Acad., Dordrecht, Netherlands.
Piété, H., L. Marié, B. Marsset, Y. Thomas, and M.-A. Gutscher (2013), Seismic reflection imaging of shallow oceanographic structures, *J. Geophys. Res. Oceans*, *118*, 2329–2344, doi:10.1002/jgrc.20156.
Ruddick, B., H. B. Song, C. Z. Dong, and L. Pinheiro (2009), Water column seismic images as maps of temperature gradient, *Oceanography*, *22*, 192–205.
Sallarès, V., B. Biescas, G. Buffett, R. Carbonell, J. J. Dañobeitia, and J. L. Pelegrí (2009), Relative contribution of temperature and salinity to ocean acoustic reflectivity, *Geophys. Res. Lett.*, *36*, L00D06, doi:10.1029/2009GL040187.
Soloviev, A. V., N. V. Vershinsky, and V. A. Bezverchnii (1988), Small-scale turbulence measurements in the thin surface layer of the ocean, *Deep Sea Res., Part A*, *35*(N12A), 1859–1874.
Thomas, Y., B. Marsset, L. Marié, S. Ker, and H. Piété (2013), Compte rendu de mission: Mission ifosismo, n/o le côtes de la manche 20–23 septembre 2012. Adéquation de la source sismique sparker à l'imagerie de la thermocline en mer d'iroise, technical report, PDG/REM/GM/EIS-08022013-01, IFREMER, Brest.
Wenz, G. M. (1962), Acoustic ambient noise in the Ocean: Spectra and sources, *J. Acoust. Soc. Am.*, *34*(12), 1936–1956.
Yilmaz, O. (1987), *Seismic Data Processing*, Soc. of Explor. Geophys., Tulsa, Okla.

 © 2015. American Geophysical Union. All Rights Reserved.